nature photonics

LETTERS

https://doi.org/10.1038/s41566-021-00789-9

Check for updates

Scattering invariant modes of light in complex media

Pritam Pai[1], Jeroen Bosch[1], Matthias Kühmayer[2], Stefan Rotter[2]✉ and Allard P. Mosk[1]✉

Random scattering of light in disordered media is an intriguing phenomenon of fundamental relevance to various applications[1]. Although techniques such as wavefront shaping and transmission matrix measurements[2,3] have enabled remarkable progress in advanced imaging concepts[4–11], the most successful strategy to obtain clear images through a disordered medium remains the filtering of ballistic light[12–14]. Ballistic photons with a scattering-free propagation are, however, exponentially rare and no known method has been able to increase their proportion. To address these limitations, we introduce and experimentally implement a new set of optical states that we term scattering invariant modes, whose transmitted field pattern is the same, irrespective of whether they scatter through a disordered sample or propagate ballistically through a homogeneous medium. We observe scattering invariant modes that are only weakly attenuated in dense scattering media, and show in simulations that their correlations with the ballistic light can be used to improve imaging inside scattering materials.

The concept of transmission eigenchannels in scattering media[15,16] has greatly expanded both our understanding of light transport[3,17–21] and our ability to engineer the delivery of radiation across disordered materials[2,22–25]. Although the occurrence and the statistics of these channels has been well described by random matrix theories[16,26], the ballistic contributions to the transmission process are much harder to capture by such tools. We introduce here a set of scattering invariant modes (SIMs) that embody the defining feature of ballistic light, and are transmitted through a disordered medium in the same way as through homogeneous space (Fig. 1). To capture this property for constructing SIMs based on experimentally accessible quantities, we employ the corresponding transmission matrices for a scattering medium (T_s) and for a scattering-free volume of air (T_{air}). The input electric fields of SIMs (denoted as $\tilde{\mathbf{E}}$) are then just determined by the requirement that their output field patterns are the same, irrespective of which one of the two transmission matrices is used to propagate the field from the input to the output. Expressing the in- and outgoing fields as vectors of complex coefficients that represent the horizontal and vertical field components in a suitable basis set results in the following constitutive relation for SIMs:

$$T_s\tilde{\mathbf{E}}_n = \alpha_n T_{air}\tilde{\mathbf{E}}_n \,. \tag{1}$$

This generalized linear eigenvalue problem demonstrates that SIMs emerge as a complete (though not orthogonal) set of input states $\tilde{\mathbf{E}}_n$, where n enumerates the states. These states are tailored to T_s and characterized each by a SIM eigenvalue α_n. The complex value of α_n quantifies the global amplitude (phase) by which the output field of the corresponding SIM eigenstate $\tilde{\mathbf{E}}_n$ is attenuated (phase-shifted) when transmitted through the medium rather than through air. To obtain an eigenvalue equation that is numerically stable, we multiply both sides with the Hermitian conjugate of the matrix T_{air}, which is unitary in theory and approximately so in experiment, resulting in the SIM eigenvalue equation

$$T_{air}^{\dagger}T_s\tilde{\mathbf{E}}_n = \alpha_n\tilde{\mathbf{E}}_n \,. \tag{2}$$

In this form we see that SIMs are invariant in shape under the operation of forward propagation in the scattering medium followed by backpropagation in air.

To implement this concept in practice, we first measured both T_{air} and T_s, and inserted them in equation (2). We measured polarization-complete matrices to maximize the level of control over the light field. To generate the resulting coherent fields with controllable amplitude, phase and polarization ellipse on a two-dimensional grid of pixels, we constructed a vector wavefront synthesizer[27]. A microscope objective projects the pixel array onto the sample surface. The transmitted light is collected by a second microscope objective and recorded by a vector wavefront analyser, which measures amplitude, phase and polarization ellipse on a similar 2D array of pixels. The measurement and analysis method is reported in detail in ref. [28] and in Supplementary Section 1.

Our scattering sample consisted of a layer of zinc oxide (ZnO) nanopowder deposited on a glass slide, part of which was cleaned to act as a scattering-free reference medium. The scattering layer was inspected to verify the absence of holes. The sample was mounted on a calibrated translation stage to reversibly exchange the sample for a clean substrate.

In a first demonstration, we used a scattering sample with a thickness of $1.6(\pm0.5)\,\mu$m, corresponding to about two mean free paths (for these subwavelength scatterers, the scattering mean free path ℓ equals the transport mean free path ℓ_t). The ballistic transmission was only 12%, as found from the diagonal elements of the transmission matrix. In Fig. 2a–d we show the transmitted field of a SIM with $|\alpha|=0.64$ projected through both media using the vector wavefront synthesizer. The measured intensity transmittance of this state was 31%, which (due to imperfect projection) is lower than the ideal transmittance $|\alpha|^2=0.41$. The fields transmitted through air ($\mathbf{E}_{air}$) and the scattering medium ($\mathbf{E}_{scat}$) were visually very similar in both polarization components, quantified by a normalized field overlap (cosine similarity) of $|\mathbf{E}_{scat}^{*}\cdot\mathbf{E}_{air}|/(|\mathbf{E}_{scat}||\mathbf{E}_{air}|)=0.79$. The measured cosine similarity for all the projected SIMs, displayed in Fig. 2e, showed a strong dependence on $|\alpha|$. We found that the similarity increased monotonically with $|\alpha|$ to reach values up to about 0.82. Ideally, one would expect the cosine similarity between SIMs projected through the different media to be unity. In the experiment,

[1]Debye Institute for Nanomaterials Science and Center for Extreme Matter and Emergent Phenomena, Utrecht University, Utrecht, the Netherlands. [2]Institute for Theoretical Physics, TU Wien, Vienna, Austria. ✉e-mail: stefan.rotter@tuwien.ac.at; a.p.mosk@uu.nl

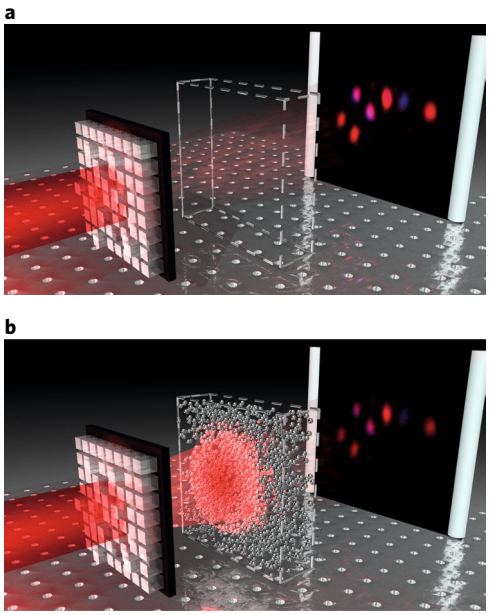

Fig. 1 | Illustration of the concept. a,**b**, A SIM is generated by a spatial light modulator and propagates through empty space (**a**) and a scattering sample (**b**). The spatial light modulator is configured identically in both cases. The SIM is defined so that its transmitted field remains unchanged by the presence of the disordered medium apart from a reduction in overall brightness and a global phase shift, expressed by the complex SIM eigenvalue α.

the effects of noise, imperfect projection and the non-unitarity of the experimental T_{air} reduced this value, especially for low $|\alpha|$.

The complex SIM eigenvalue spectrum is shown in Fig. 2f. The phase of α in this diffuse spectrum is distributed approximately isotropically. The density of eigenvalues gradually decays with distance from the origin until around $|\alpha| = 0.66$, corresponding to 3.5 times the ordinary ballistic transmission. For comparison, we show in Fig. 2g the eigenvalue spectrum of a complex Gaussian random matrix with the same average transmission, which is homogeneous inside a sharply bounded Ginibre disk[29]. Further statistics of the measured transmission matrix can be found in Supplementary Section 2.

In Fig. 2h we show the complex eigenvalue spectrum of the numerically calculated matrix $T_{air}^{\dagger} T_s$ of a sample of one mean free path in thickness, which included the effect of the finite NA of the objectives[30]. We observed a non-uniform distribution similar to the experimental data. The deviation of both the experimental and the simulated data from the eigenvalue spectrum of a random matrix shows that the eigenvalues reflect the sample-specific details of the scattering process. The occurrence of relatively large SIM eigenvalues, which are exponentially rare in random matrix theory[29], is particularly noteworthy as the corresponding SIMs feature output speckle patterns with the largest similarity values and with the highest transmission through the scattering sample.

In many cases, one is only interested in the field transmitted into a few modes, such as pixels making up a sparse image. We generated the corresponding sparse SIMs by numerically backpropagating the sparse target field through the sample (by applying the experimentally measured $T_s^{\dagger}$) and separately through the reference (by applying the experimentally measured $T_{air}^{\dagger}$) and superposing the

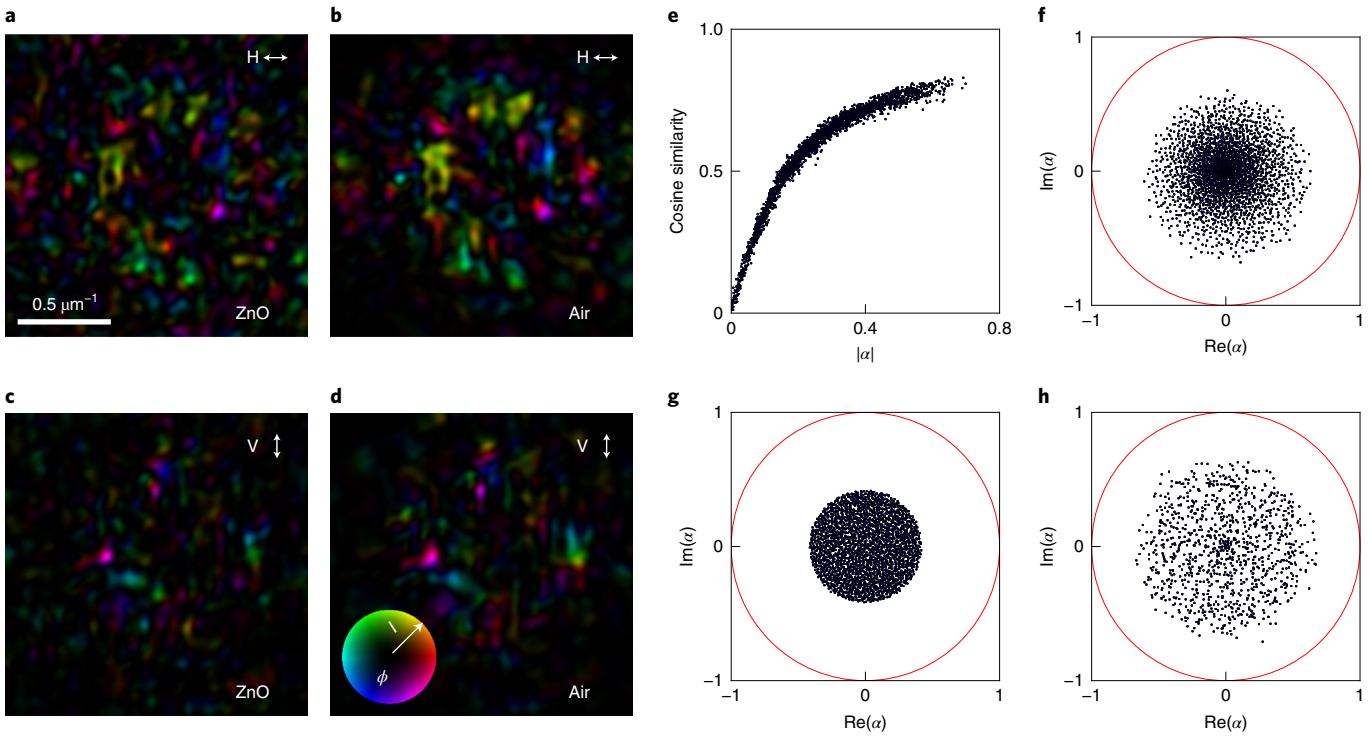

Fig. 2 | Experimentally transmitted SIMs and their statistics. a–**d**, Far field of a SIM transmitted through a layer of ZnO (**a**,**c**) or through the same thickness of air (**b**,**d**) in the horizontal (**a**,**b**) and vertical (**c**,**d**) polarization components, respectively. The colour represents phase ϕ and the brightness represents amplitude I, as shown in the inset in **d**. The associated cosine similarity of the fields is 0.79 and the SIM eigenvalue is $|\alpha| = 0.64$. **e**, Cosine similarity of all SIMs propagated through air and through the scattering medium versus $|\alpha|$. **f**, The complex generalized eigenvalue spectrum determined from the measured TMs. The unit circle is shown in red. **g**, Numerically generated distribution of eigenvalues of a Ginibre ensemble. **h**, SIM eigenvalues from a numerical 2D simulation of a sample with a thickness of one mean free path (Methods). The scale bar in **a** also applies to **b**–**d**.

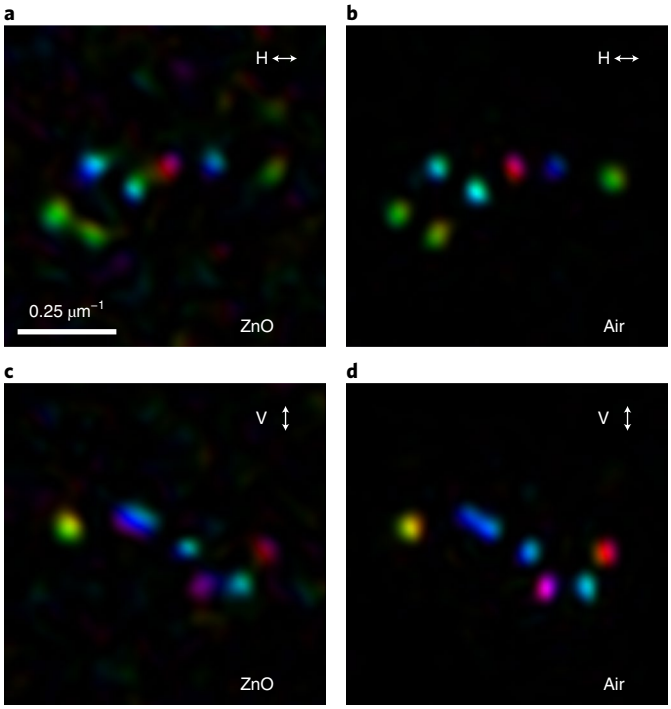

Fig. 3 | Experimental realization of a sparse SIM. a–**d**, Far field intensity of the horizontal (**a**,**b**) and vertical (**c**,**d**) polarization components of a sparse SIM transmitted through a 5.2(±0.5)-μm-thick ZnO powder (**a**,**c**) and through the same thickness of air (**b**,**d**), shaped to resemble the stellar constellations of Ursa Minor (top row) and Ursa Major (bottom row). The scale bar in **a** also applies to **b**–**d**, and the colour scheme is the same as in Fig. 2.

two (typically completely uncorrelated) incident fields thus obtained (Methods).

In Fig. 3 we show an example of a sparse SIM propagated through a ZnO powder sample and through the same thickness of air. The SIM shown here was constructed to display a point pattern for which we independently controlled the amplitude, phase and polarization in each spot. Although a low-intensity uncorrelated speckle is visible in the background, the similarity between the high-intensity spots is striking. This principle is easily generalized to propagate images with controlled phase and polarization through two different complex media using only one incident field.

Several transmission matrix-based methods have proved valuable for imaging through scattering media. The intriguing new possibility is that SIMs allow us to improve imaging inside the complex medium. Externally, each SIM seems to propagate through a semi-transparent medium with transmittance $|\alpha|^2$ and a phase of $\arg(\alpha)$ relative to propagation through air. For sparse scattering media that have scatter-free areas, we show in Supplementary Section 3 that SIMs with high values of $|\alpha|$ preferentially propagate through the scatter-free areas, just like ballistic light would do inside the medium.

Inside dense scattering media without holes or gaps, we find, using both 2D and 3D wave simulations, that SIMs remain correlated with the ballistic component of the incident light up to a depth z of several mean free paths, but are gradually shifted in phase and amplitude as they propagate. In Supplementary Section 4 we show numerically that the phase shift they accrue while propagating to depth z inside the medium of thickness L turns out to be well described by $\arg(\alpha)\times z/L$. By compensating this phase shift, we synthesized a 'SIM-corrected' wave that focused better than an uncorrected wavefront deep inside the scattering sample. Specifically, to produce a focus at depth z inside the sample, we first backpropagated an ideal focus to the input surface using the known air transmission

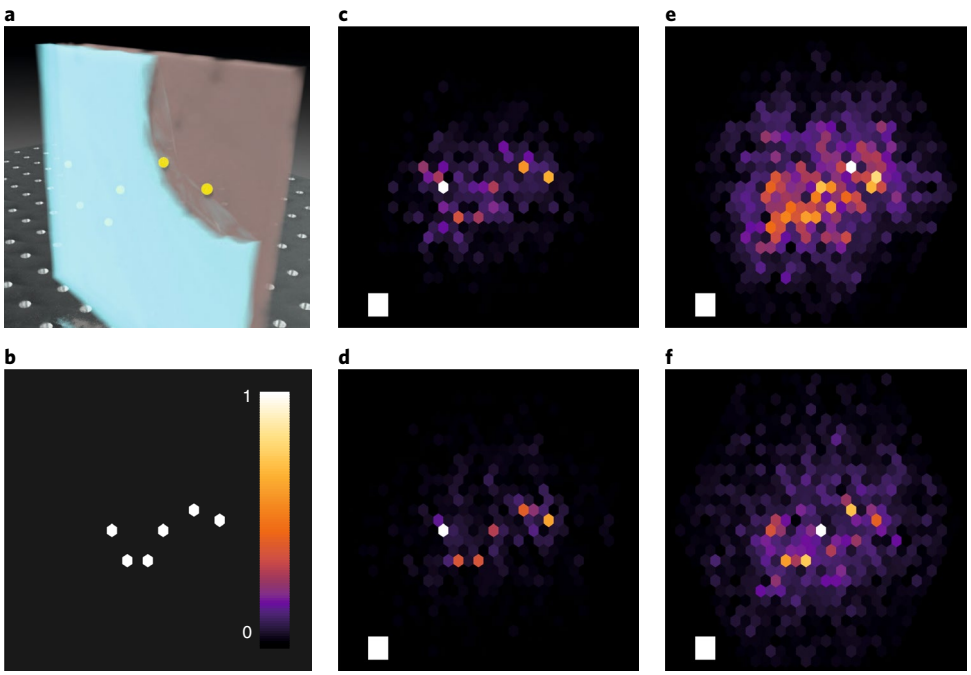

Fig. 4 | Simulations of imaging using SIMs. a, Sketch of the simulation set-up: a fluorescent object is sandwiched between two scattering layers (one is peeled back for clarity) each of thickness $L/2$. **b**, The simulated object, consisting of six point-like particles. The inset shows the intensity colour scale used in panels **b**–**f**. **c**,**d**, Uncorrected (**c**) and corrected (**d**) images of the object using SIMs for a system thickness of $L = 5.4\ell$. **e**,**f**, Uncorrected (**e**) and corrected (**f**) images for $L = 7.1\ell$. The squares indicate the size of the wavelength in the simulation.

Table 1 | Quantifying the use of SIMs for deep imaging

Thickness L/ℓ	$C_{uncorr.}$	C_{SIM}	N
5.4	0.728 (0.03)	0.802 (0.03)	23
7.1	0.500 (0.07)	0.606 (0.07)	50
9.0	0.326 (0.07)	0.395 (0.09)	52

The mean Pearson's correlation coefficients C between images (uncorrected and SIM-corrected) and the true object are shown with the standard deviation in parentheses, averaged over N different disorder configurations.

matrix $T_{air}(z)$ from the surface to the scattering layer at depth z. We then decomposed the backpropagated focus field into SIMs, which were then individually corrected by the phase shift expected for their specific values of α and z. An amplitude correction provided more weight to those SIMs with small phases of α since they feature a higher fidelity with respect to the field in the reference medium. These adjusted SIM amplitudes then entered the corrected incident field (see Supplementary Sections 4 and 5 for full details) and were numerically propagated through the scattering medium to check their focusing performance with respect to the uncorrected field. Importantly, our correction procedure solely relied on data from the experimentally accessible external transmission matrix[31].

In Fig. 4 we show typical simulation results for scanning excitation imaging of a fluorescent object sandwiched between two scattering layers, as depicted in Fig. 4a,b. The layers are strongly and isotropically scattering, with ℓ of about 4 wavelengths. Already in the most optically thin case considered here, the uncorrected image in Fig. 4c is heavily distorted by speckle.

In Fig. 4d we demonstrate the effect that the SIM-based correction of the excitation beam had using the procedure described above. Figure 4e,f shows the corresponding images for a more strongly scattering system. The improvement in imaging was quantified by the correlation coefficient between the recovered image and the true object averaged over many realizations, as detailed in Table 1. We see that a statistically significant improvement in image quality was possible up to a large thickness of $L=9\ell$. SIM-based correction of the incident wave may be combined with confocal detection or multiphoton methods to allow even deeper imaging.

In summary, we introduce the concept of SIMs, which produce the same transmitted field profile through a multiple scattering sample as when propagating through a reference medium. We successfully generate SIMs experimentally and find a high similarity between the fields propagated through a layer of ZnO powder and through the same thickness of air. We show explicitly how to use this feature to achieve free-space transmission of simple images across strongly disordered media. Moreover, SIMs remain correlated with the ballistic light inside a medium and can be used to improve imaging quality under difficult conditions. These remarkable properties make SIMs an attractive new set of tools both from a fundamental perspective and for applications in imaging through complex media.

Online content

Any methods, additional references, Nature Research reporting summaries, source data, extended data, supplementary information, acknowledgements, peer review information; details of author contributions and competing interests; and statements of data and code availability are available at https://doi.org/10.1038/s41566-021-00789-9.

Received: 30 June 2020; Accepted: 3 March 2021;
Published online: 8 April 2021

References

1. Johnson, C. & Gabriel, D. *Laser Light Scattering* (Dover Publications, 2015).
2. Mosk, A. P., Lagendijk, A., Lerosey, G. & Fink, M. Controlling waves in space and time for imaging and focusing in complex media. *Nat. Photon.* **6**, 283–292 (2012).
3. Rotter, S. & Gigan, S. Light fields in complex media: mesoscopic scattering meets wave control. *Rev. Mod. Phys.* **89**, 015005 (2017).
4. Yoon, S. et al. Deep optical imaging within complex scattering media. *Nat. Rev. Phys.* **2**, 141–158 (2020).
5. Kubby, J., Gigan, S. & Cui, M. (eds) *Wavefront Shaping for Biomedical Imaging* (Cambridge Univ. Press, 2019).
6. Bertolotti, J. et al. Non-invasive imaging through opaque scattering layers. *Nature* **491**, 232–234 (2012).
7. Katz, O., Heidmann, P., Fink, M. & Gigan, S. Non-invasive single-shot imaging through scattering layers and around corners via speckle correlations. *Nat. Photon.* **8**, 784–790 (2014).
8. Kang, S. et al. High-resolution adaptive optical imaging within thick scattering media using closed-loop accumulation of single scattering. *Nat. Commun.* **8**, 2157 (2017).
9. Jang, M. et al. Wavefront shaping with disorder-engineered metasurfaces. *Nat. Photon.* **12**, 84–90 (2018).
10. Horisaki, R., Mori, Y. & Tanida, J. Incoherent light control through scattering media based on machine learning and its application to multiview stereo displays. *Opt. Rev.* **26**, 709–712 (2019).
11. Badon, A. et al. Distortion matrix concept for deep optical imaging in scattering media. *Sci. Adv.* **6**, eaay7170 (2020).
12. Wang, L. V. & Wu, H. *Biomedical Optics: Principles and Imaging* (Wiley, 2007).
13. Ntziachristos, V. Going deeper than microscopy: the optical imaging frontier in biology. *Nat. Methods* **7**, 603–614 (2010).
14. Drexler, W. & Fujimoto, J. (eds) *Optical Coherence Tomography: Technology and Applications* (Springer International Publishing, 2015).
15. Dorokhov, O. On the coexistence of localized and extended electronic states in the metallic phase. *Solid State Commun.* **51**, 381–384 (1984).
16. Beenakker, C. W. J. Random-matrix theory of quantum transport. *Rev. Mod. Phys.* **69**, 731–808 (1997).
17. Pendry, J., MacKinnon, A. & Pretre, A. Maximal fluctuations—a new phenomenon in disordered systems. *Phys. A* **168**, 400–407 (1990).
18. Akkermans, E. & Montambaux, G. *Mesoscopic Physics of Electrons and Photons* (Cambridge Univ. Press, 2007).
19. Pena, A., Girschik, A., Libisch, F., Rotter, S. & Chabanov, A. A. The single-channel regime of transport through random media. *Nat. Commun.* **5**, 3488 (2014).
20. Davy, M., Shi, Z., Wang, J. & Genack, A. Z. Transmission statistics and focusing in single disordered samples. *Opt. Express* **21**, 10367–10375 (2013).
21. Miller, D. A. B. Waves, modes, communications and optics. *Adv. Opt. Photon.* **11**, 679–825 (2019).
22. Vellekoop, I. M. & Mosk, A. P. Universal optimal transmission of light through disordered materials. *Phys. Rev. Lett.* **101**, 120601 (2008).
23. Hsu, C. W., Liew, S. F., Goetschy, A., Cao, H. & Stone, A. D. Correlation-enhanced control of wave focusing in disordered media. *Nat. Phys.* **13**, 497–502 (2017).
24. Yu, H. et al. Measuring large optical transmission matrices of disordered media. *Phys. Rev. Lett.* **111**, 153902 (2013).
25. Kim, M. et al. Maximal energy transport through disordered media with the implementation of transmission eigenchannels. *Nat. Photon.* **6**, 581–585 (2012).
26. Mello, P., Pereyra, P. & Kumar, N. Macroscopic approach to multichannel disordered conductors. *Ann. Phys.* **181**, 290–317 (1988).
27. Bosch, J., Goorden, S. A. & Mosk, A. P. Frequency width of open channels in multiple scattering media. *Opt. Express* **24**, 26472 (2016).
28. Pai, P., Bosch, J. & Mosk, A. P. Optical transmission matrix measurement sampled on a dense hexagonal lattice. *OSA Continuum* **3**, 637–648 (2020).
29. Forrester, P. J. & Nagao, T. Eigenvalue statistics of the real Ginibre ensemble. *Phys. Rev. Lett.* **99**, 050603 (2007).
30. Goetschy, A. & Stone, A. D. Filtering random matrices: the effect of incomplete channel control in multiple scattering. *Phys. Rev. Lett.* **111**, 063901 (2013).
31. Popoff, S. M. et al. Measuring the transmission matrix in optics: an approach to the study and control of light propagation in disordered media. *Phys. Rev. Lett.* **104**, 100601 (2010).

Methods

Vector wavefront analyser. The transmitted field is measured with angle-offset holography[32], for both polarization components separately. The speckle field transmitted through the scattering sample was collected with a high-numerical aperture (NA) immersion objective (NA = 1.4). The two polarization components were imaged on separate cameras, and interfered with a reference beam that was incident at a small angle. The local amplitude and phase were calculated from the interference pattern.

The TM measurements were carried out by sending incident waves with 1,141 different wavevectors, on a hexagonal grid in k-space, for two orthogonal polarizations. The transmitted amplitudes were resampled to the same basis set, yielding matrices of dimension 2,282 × 2,282. Both the incident and the transmitted fields were sampled on a hexagonal lattice in Fourier space with a lattice constant chosen to minimize overlap between adjacent lattice points.

Construction of sparse SIMs. Sparse SIMs emerged from the medium as a sparse field coupling to a relatively small number M modes of interest. For simplicity, we assumed that these modes corresponded to waves E_i focused on target points $\{y_i\}$. The basis of incident waves was chosen to be $\{u_i,v_i\}$, with $\mathbf{u}_i = T_{\mathrm{air}}^{\dagger}\mathbf{E}_i/|T_{\mathrm{air}}^{\dagger}\mathbf{E}_i|$ and $\mathbf{v}_i = T_{\mathrm{s}}^{\dagger}\mathbf{E}_i/|T_{\mathrm{s}}^{\dagger}\mathbf{E}_i|$; that is, this basis contained the waves that were optimally focused on the target points[22] either through the air or through the sample. Assuming that $M \ll N$ and that the target modes were non-overlapping, the dot product between u_i and v_i can be neglected, and we had $T_{\mathrm{s}}\mathbf{v}_i \approx \bar{T}E_i$, where $\bar{T}$ is the average transmission of the scattering sample[22]. Similarly, $T_{\mathrm{air}}\mathbf{u}_i \approx \mathbf{E}_i$ as the air has transmission unity. Under these assumptions, an approximate SIM could be constructed as $\mathbf{E}_{\mathrm{in}}(\alpha) = c\sum_i(\mathbf{u}_i + \alpha\mathbf{v}_i/\bar{T})$. Here, c is a normalization constant and α is the desired generalized eigenvalue. The procedure is equivalent to taking a weighted sum of a field shaped to project the image through air and a field shaped to project the same image through the scattering sample.

Numerical simulations. We numerically solved the 2D scalar Helmholtz equation $[\Delta + n^2(\mathbf{r})k_0^2]\psi(\mathbf{r}) = 0$ using the finite element method[33] (https://ngsolve.org), where Δ is the Laplacian in two dimensions, $n(\mathbf{r})$ is the refractive index distribution, $\mathbf{r} = (x,y)$ is the position vector, $k_0 = 2\pi/\lambda$ is the free-space wavenumber with λ being the wavelength and $\psi(\mathbf{r})$ is the z component of the transverse-electric (TE)-polarized electric field.

To model the experimental systems, we used a scattering region that was longitudinally and transversally attached to leads featuring hard-wall boundary conditions to use a waveguide mode basis, where we used $k_0 = 2\pi/\lambda = 1{,}000.5\pi/W$ where W is the width of the longitudinal input and output lead. Perfectly matched layers were then added to these open ends to absorb the outgoing waves without any backreflections, thus mimicking semi-infinite leads. As the scattering matrix was only calculated between the input and output ports, the remaining perfectly matched layers at the top and bottom leads of our geometry served as loss channels arising in the experiment due to a limited NA. L was then adjusted according to the wavelength in the experiment; that is, we used the same ratio of L/λ as in the experiment. The ZnO nanoparticles were modelled by circular scatterers with a refractive index of $n_{\mathrm{scat}} = 2$, where their diameter was again of the same ratio $d_{\mathrm{scat}}/\lambda$ as in the experiment. As these ZnO nanoparticles tended to stick together, we mimicked this behaviour by using circular scatterers of larger sizes.

The densely filled samples in Fig. 2 were simulated with a scattering region of length $L = \lambda(L^{\mathrm{exp}}/\lambda^{\mathrm{exp}})$, where $L^{\mathrm{exp}} = 2.1\,\mu\mathrm{m}$, which was 40% filled with circular scatterers whose diameters were $d_{\mathrm{scat}} = n\lambda(d_{\mathrm{scat}}^{\mathrm{exp}}/\lambda^{\mathrm{exp}})$. Here, $d_{\mathrm{scat}}^{\mathrm{exp}} \approx 200\,\mathrm{nm}$, $\lambda^{\mathrm{exp}} = 633\,\mathrm{nm}$ and $n = 1,2$, where we chose that every scatterer size filled out the same fraction of the total area of the scattering region. To simulate free space, we removed all the scatterers, leaving us with an empty scattering region in which waves could escape through the transversally added leads featuring perfectly matched layers that absorb the outgoing waves.

Finally, we used mesoscopic transport theory to calculate the scattering matrices of these systems between the input and the output leads, which were then used to calculate the scattering invariant modes from equation (2).

Data availability

The data that underlie the plots within this paper and other findings of this study are available from the corresponding authors on reasonable request.

Code availability

The code used to generate simulated data and plots is available from the corresponding authors on reasonable request.

References

32. Cuche, E., Marquet, P. & Depeursinge, C. Spatial filtering for zero-order and twin-image elimination in digital off-axis holography. *Appl. Opt.* **39**, 4070–4075 (2000).
33. Schöberl, J. *C++11 Implementation of Finite Elements in NGSolve* (Institute for Analysis and Scientific Computing, Vienna Univ. Technology, 2014).

Acknowledgements

We acknowledge helpful discussions with P. Ambichl, D. Bouchet, S. Faez, D. van Oosten, P. Jurrius, D. Killian, C. R. de Kok, F. Salihbegovic and S. Steinhauer. Financial support was provided by the Austrian Science Fund (FWF) under project WAVELAND (grant number P32300 to S.R.) and by the Netherlands Organization for Scientific Research NWO (grant number Vici-68047618 to A.P.M.). The computational results presented in this paper were achieved using the Vienna Scientific Cluster (VSC).

Author contributions

The experiments were designed by A.P.M., P.P. and J.B. and implemented by P.P. and J.B. The 2D full-wave numerical simulations and the theoretical analysis were carried out by M.K. and the 3D calculations by A.P.M. S.R. proposed the idea and supervised the theoretical research. All authors analysed the results and contributed to the writing of the manuscript.

Competing interests

The authors declare no competing interests.

Additional information

Supplementary information The online version contains supplementary material available at https://doi.org/10.1038/s41566-021-00789-9.

Correspondence and requests for materials should be addressed to S.R. or A.P.M.

Peer review information *Nature Photonics* thanks Roarke Horstmeyer and the other, anonymous, reviewer(s) for their contribution to the peer review of this work.

Reprints and permissions information is available at www.nature.com/reprints.